A&A 503, 577–587 (2009)
DOI: 10.1051/0004-6361/200811595
© ESO 2009

Astronomy & Astrophysics

The solar chromosphere at high resolution with IBIS

IV. Dual-line evidence of heating in chromospheric network

G. Cauzzi[1,2], K. Reardon[1,2], R. J. Rutten[2,3,4], A. Tritschler[2], and H. Uitenbroek[2]

[1] INAF – Osservatorio Astrofisico di Arcetri, Largo Enrico Fermi 5, 50125 Firenze, Italy
e-mail: gcauzzi@arcetri.astro.it
[2] NSO/Sacramento Peak, PO Box 62, Sunspot, NM 88349–0062, USA
[3] Sterrekundig Instituut, Utrecht University, Postbus 80 000, 3508 TA Utrecht, The Netherlands
[4] Institute of Theoretical Astrophysics, University of Oslo, PO Box 1029, Blindern, 0315 Oslo, Norway

Received 24 December 2008 / Accepted 10 June 2009

ABSTRACT

The structure and energy balance of the solar chromosphere remain poorly known. We used the imaging spectrometer IBIS at the Dunn Solar Telescope to obtain fast-cadence, multi-wavelength profile sampling of Hα and Ca II 854.2 nm over a sizable two-dimensional field of view encompassing quiet-Sun network. We provide a first inventory of how the quiet chromosphere appears in these two lines by comparing basic profile measurements in the form of image displays, temporal-average displays, time slices, and pixel-by-pixel correlations. We find that the two lines can be markedly dissimilar in their rendering of the chromosphere, but that, nevertheless, both show evidence of chromospheric heating, particularly in and around network: Hα in its core width and Ca II 854.2 nm in its brightness. We discuss venues for improved modeling.

Key words. Sun: photosphere – Sun: chromosphere – Sun: magnetic fields – Sun: faculae, plages

1. Introduction

The solar chromosphere is one of the most difficult solar atmospheric regimes to observe, model, and understand (see recent reviews by Judge & Peter 1998; Judge 2006; Carlsson 2007; Rutten 2007). In this paper we compare spectrally resolved chromospheric image sequences taken in the Balmer Hα line at 656.3 nm and the Ca II 854.2 nm line (henceforth abbreviated to Ca IR). Both lines sample the chromosphere, but in different manners, such that combining them yields richer diagnostics than when using either line alone. This has not been done with the angular, spectral, and temporal resolution and coverage furnished by the imaging spectroscopy presented here. In this initial paper we compare the chromospheric scenes seen in the two lines by displaying basic spectral measurements across a quiet-sun field of view. In particular, we show that both lines provide evidence of network heating, each in its own manner. So far, chromospheric heating in or above the magnetic concentrations that cluster together to constitute the network has been most clearly evident as brightness enhancement of the cores of Ca II H & K. A recent discussion of its nature is given by Hasan & van Ballegooijen (2008). Additional information from other diagnostics is obviously desirable.

There is an extended literature addressing chromospheric physics using filtergrams taken in Hα or Ca II H & K, while most work using Ca IR was performed with one-dimensional spectrometry. We obtain a fresh view by combining Hα and Ca IR in imaging spectroscopy, obtaining high angular resolution with adaptive optics at the Dunn Solar Telescope (DST) at the US National Solar Observatory/Sacramento Peak and excellent spectral profile sampling by employing the Interferometric Bi-dimensional Spectrometer (IBIS) mounted at this telescope.

High-resolution imaging spectroscopy in Ca IR was initiated with IBIS in the study of Vecchio et al. (2007) and continued in the previous papers of this series (Cauzzi et al. 2008; Vecchio et al. 2009; Reardon et al. 2009) mostly addressing the properties of the quiet chromosphere. Recent chromospheric studies with the Swedish 1-m Solar Telescope combine high cadence with 0.2 arcsec resolution but employed Hα only in single-wavelength filtergraph sampling (e.g., Hansteen et al. 2006; van Noort & Rouppe van der Voort 2006; De Pontieu et al. 2007a; Rouppe van der Voort et al. 2007). The Dutch Open Telescope has registered many Hα filtergram sequences with subarcsecond resolution (e.g., Rutten et al. 2008) but only with coarse profile sampling and limited in duration by atmospheric seeing. Much longer multi-wavelength Hα filtergram sequences at this resolution were expected from the tunable filtergraph onboard *Hinode*, but technical problems have severely limited its ability to sample the Hα profile at high cadence. The capability of IBIS and similar new Fabry-Pérot instruments (the new Göttingen FPI at the German Vacuum Tower Telescope described by Bello González & Kneer 2008; and CRISP at the SST following the design of Scharmer 2006) to supply high-resolution imaging at fast cadence, with full profile sampling of both lines, and over fairly long durations represents a major step forward in investigations of the solar chromosphere.

Our goal here is to show and compare what the quiet chromosphere looks like at such improved resolution and coverage of space, time, and wavelength in the two lines. Comparison between the two is of interest because their formation differs intrinsically, as discussed in Sect. 4.1. Each has its advantages and disadvantages as a chromospheric diagnostic. We limit the analysis here to a straightforward presentation of three basic profile measurements: the profile-minimum intensity, the Dopplershift

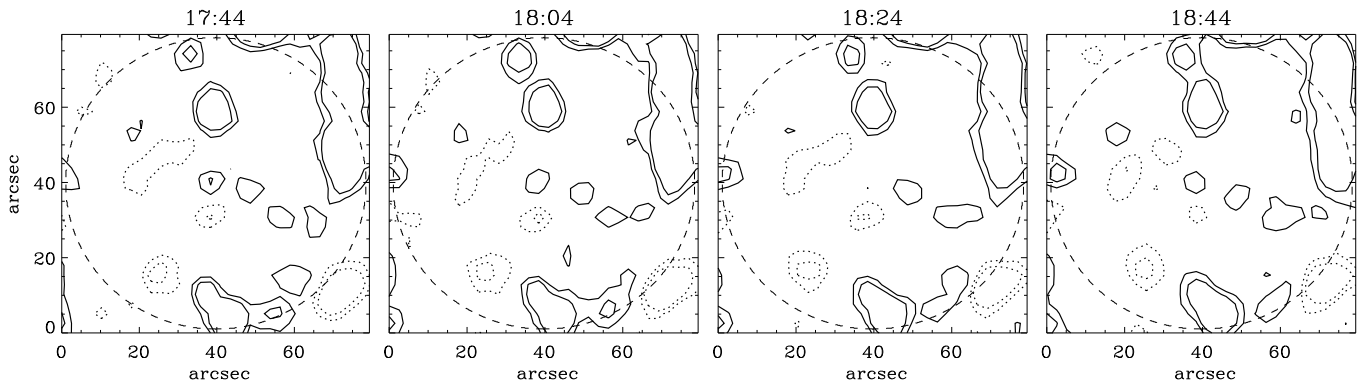

Fig. 1. Magnetic field evolution for the IBIS field of view (dashed circle), from GONG data at http://gong.nso.edu, at 20-min intervals. The time of observation is specified at the top of each panel. The IBIS run was from 17:50 to 18:40 UT. The contours show the apparent magnetic flux density at values of 10 and 20 Mx cm^{-2}, for positive (solid) and negative (dotted) polarity.

Table 1. IBIS profile scan parameters.

Line	Hα	Ca IR
Nominal wavelength [nm]	656.281	854.214
Instrumental profile FWHM [pm]	2.2	4.4
Wavelength range [nm]	0.21	0.18
Core sampling interval [nm]	0.01	0.008
Number of wavelength steps	22	20
Profile scan duration [s]	5.2	4.7

of the profile mimimum, and the line-core width. Comparison of the general appearance of the two lines in these basic properties already yields informative similarities and differences.

2. Observations, data reduction and profile measurements

The imaging spectrometer IBIS is mounted at one of the two high-order adaptive-optics feeds at the DST. The latter, described by Rimmele (2004), serves to stabilize the image and correct wavefront deformations in real time. IBIS consists of two Fabry-Pérot interferometers in tandem and delivers sequences of narrowband images with the passband stepping quickly through multiple selectable spectral lines. IBIS is detailed in Cavallini (2006) and Reardon & Cavallini (2008).

In this paper we use data taken during 17:50−18:40 UT on 15 March 2007. Table 1 specifies the spectral profile sampling. IBIS acquired 192 spectral image sets sampling the Hα, Ca IR and Fe I 709.0 nm lines with a cadence of 15.4 s between successive scans of all three lines. The Fe I data are not considered in this paper. Hα was scanned with a constant spectral sampling interval of 0.01 nm, Ca IR with 0.008 nm sampling in the core and in each wing at three wavelengths separated by 0.016 nm.

The circular field of view has a diameter of 80 arcsec and was located near disk center at heliocentric coordinates 3.0 S, 10.1 W degrees, $\mu = 0.98$, slightly eastward of a small bipolar plage. Figure 1 shows the magnetic content and evolution of the area from full-disk GONG magnetograms. It was very quiet, containing a few bipolar patches of magnetic concentrations that appear as bright points in simultaneously taken G-band images. Only slight topology changes occurred during the acquired sequence.

All images were corrected with appropriate dark and flat field calibrations. The transmission profile of the prefilter was measured and removed, resulting in good agreement between the spatio-temporal averages over the full sequence and the corresponding profiles in the NSO/FTS solar spectrum atlas of Wallace et al. (1998; compare also the average Ca IR profile in Cauzzi et al. 2008).

In order to retrieve the line profile at each pixel, it is necessary to accurately align the images making up a spectral scan through a line, including "rubber-sheet" destretching to correct remaining field-dependent deformations by seeing. The reference for such alignment was generated from a sequence of broadband images obtained simultaneously with the narrowband images. The best broadband image every 15 s (i.e., during each full scan of all three lines) was found by measuring granular contrast. These 192 best broad-band images per spectral set were then co-aligned to each other, including destretching through local cross-correlation while taking care not to remove persistent solar flows. The destretched sequence was Fourier filtered in both space and time using a subsonic filter to remove the Fourier components corresponding to apparent horizontal motions faster than the photospheric sound speed (7 km s^{-1}). This resulted in a high-quality master reference sequence which was then used to evaluate the seeing-induced local image motion, again using local-correlation tracking, for each individual broadband image. The destretch vectors that were derived for each of these were finally applied to the corresponding simultaneous narrowband image. This procedure results in stable, coaligned spectral-scan image sequences and so in reliable line profiles. During the moments of best seeing the resulting image quality is close to the DST diffraction limit (0.22 arcsec for Hα, 0.28 arcsec for Ca IR).

Each individual spectral profile at each pixel in each profile scan was interpolated onto a uniform wavelength grid with 0.009 nm sampling for Hα and 0.008 nm sampling for Ca IR. The radially increasing instrumental blueshift, which results from the placement of the IBIS interferometers in a collimated mount, was also removed in this resampling. For each spectral profile we then determined the wavelength of the profile-minimum by fitting a second-order polynomial to the five spectral samples centered on the position with the smallest measured intensity. The minimum of this fit is taken as the instantaneous line center, yielding both its intensity (in relative data units) and its Dopplershift (in km s^{-1} with respect to the profile-minimum wavelength of the spatio-temporal profile average over the flat-field data).

The measurement of line width is less straightforward. The scan extents specified in Table 1 do not reach the local continua outside the lines, so that we cannot measure the profile width at a fixed fractional depth from the continuum. Furthermore, the

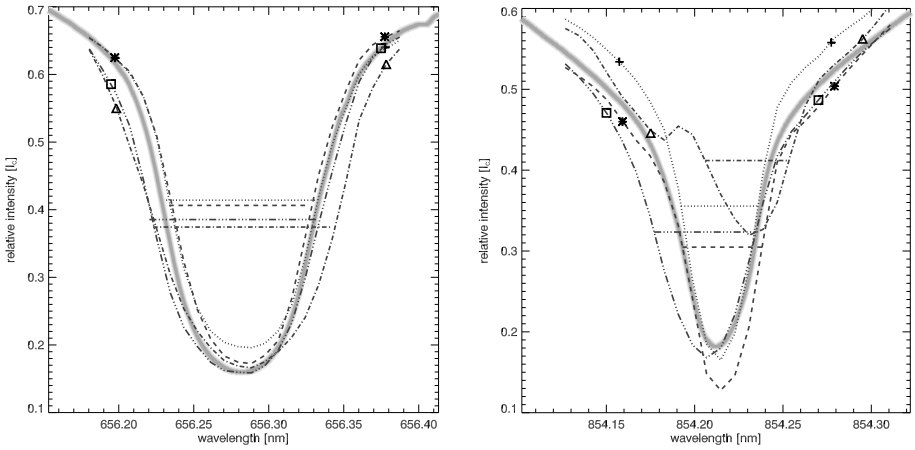

Fig. 2. Core width measurement. *Left*: Hα. *Right*: Ca IR. Each plot contains profiles from four different pixels to illustrate profile variations. The thick grey curve is the solar atlas profile. The intensity scale is in relative units with respect to the atlas continuum value. For each profile $I_\lambda(x, y, t)$ the wing intensities at given $\Delta\lambda_l$ from the profile minimum (marked by symbol pairs) are averaged. The core width is the wavelength separation of the profile samplings at half the intensity range between the profile minimum and this wing average. The same pixels are selected in Fig. 7.

shape of these chromospheric lines often varies significantly, especially in their cores. For Ca IR in particular, the extended photospheric wings tend to remain relatively stable while the chromospheric core varies dramatically. Expressing the latter's chromospheric properties in terms of photospheric continuum intensity thus is not a desirable approach. We therefore use only the inner, chromospheric part of the profile to define the property we call core width.

We evaluated these core widths per instantaneous profile per pixel by first determining and averaging the wing intensities at a specified wavelength separation $\Delta\lambda_l$ from the measured wavelength of the profile minimum. We then defined and measured the core width as the wavelength separation of the two profile flanks at half the intensity range between the minimum and this wing intensity. The separation parameter was set at $\Delta\lambda_l$ = 90 pm for Hα and $\Delta\lambda_l$ = 60 pm for Ca IR. These values were selected through inspecting many profiles with the aim to separate the chromospheric core from the photospheric wings as well as possible. The choice remains somewhat arbitrary, but we feel that this procedure is a better one than halfwidth measurements higher up in the line that would mix disparate photospheric and chromospheric contributions. Figure 2 illustrates the procedure for the Hα and Ca IR profiles from four selected pixels at one moment. Note that the Ca IR core varies much more than the Hα core, and that the highest Ca IR profile has a rather unusual redshift and blue-wing brightening to which we return below.

Finally, the observed intensities were converted into brightness temperatures by equating the spatio-temporal average of each line minimum to the corresponding absolute intensity value in the solar spectrum atlas of Neckel (1999) which is a calibrated version of the atlas of Wallace et al. (1998), and then applying the inverse of the Planck function. These formal temperatures represent kinetic temperatures only when LTE holds for the source function, which is not the case for either line (Fig. 8). The conversion serves primarily to undo the Planck-function sensitivity variation with wavelength.

3. Parameter displays and comparisons

Figure 3 shows our measurements from a single profile scan of the two lines, taken at 17:52:34 UT during one of the best-seeing moments. For each line the measurements are as specified in the previous section: the intensity of the line profile minimum expressed as brightness temperature, its Dopplershift, and the line core width defined as in Fig. 2. We describe them column by column, comparing each panel with pertinent other ones. These comparisons are quantified in the form of pixel-by-pixel correlation diagrams in the lefthand part of Fig. 6, which we describe in parallel. The diagrams are constructed from 66 spectral sets taken during very good seeing to obtain the best statistics. The caption explains the format, while the axes provide the numerical ranges of the greyscale variations in Fig. 3. The innermost contours of the diagrams in Fig. 6 represent the maxima of the overall distribution, while the curves on the top and right of each figure show the distribution of the relative quantity on each axis.

The two images of the profile-minimum intensity at left in Fig. 3 differ dramatically in their portrayal of the solar atmosphere. The corresponding scatter diagram (first panel of the second row in Fig. 6) indeed shows a total lack of brightness correlation between the two, except for the very brightest pixels. The Hα image shows masses of bright and dark chromospheric fibrils, sometimes with marked brightening towards one end. Comparison with the magnetograms in Fig. 1 shows that these bright endings correspond to the stronger magnetic concentrations, but the magnetic network pattern cannot be recognized directly from the Hα image. That is much more easily done in the Ca IR intensity image, in which the extended diffuse bright patches constituting the chromospheric network correspond reasonably well to the unsigned magnetogram distribution. The most active patch is located at the field edge at about 2 o'clock; it contributes most of the slight bright-bright correlation in Fig. 6 with brightness temperature $T_b \approx 4300$ K in both lines. The dark internetwork areas contain small-scale brightenings that last only a minute or so and mark acoustic shocks (see Movie 1 in Cauzzi et al. 2008; Vecchio et al. 2009).

We now turn to the Dopplershift maps in the center panels. The Hα Dopplermap has large similarity to the Hα profile-minimum map in its overall spatial structure. It shows the same masses of fibrils, roughly with the same bundle patterns and orientations. However, the two are dissimilar in detail: the Dopplermap fibrils tend to be shorter and they are dark or bright (moving upward or downward) without obvious relation to the contrast in the profile-minimum image, except for the brightest and the darkest features whose co-spatiality indicates exceptional downdrafts in fibril ends near the network. The lack of pixel-by-pixel similarity is quantified in the second panel of Fig. 6 which indeed shows only very slight correlation. The corresponding Ca IR diagram in the first panel of Fig. 6 shows slightly higher coherence but with negative correlation: the intensity tends to be higher at locations with larger blueshift (dark in the Dopplermap), except for the brightest pixels which therefore diminish the negative correlation in the overall Pearson

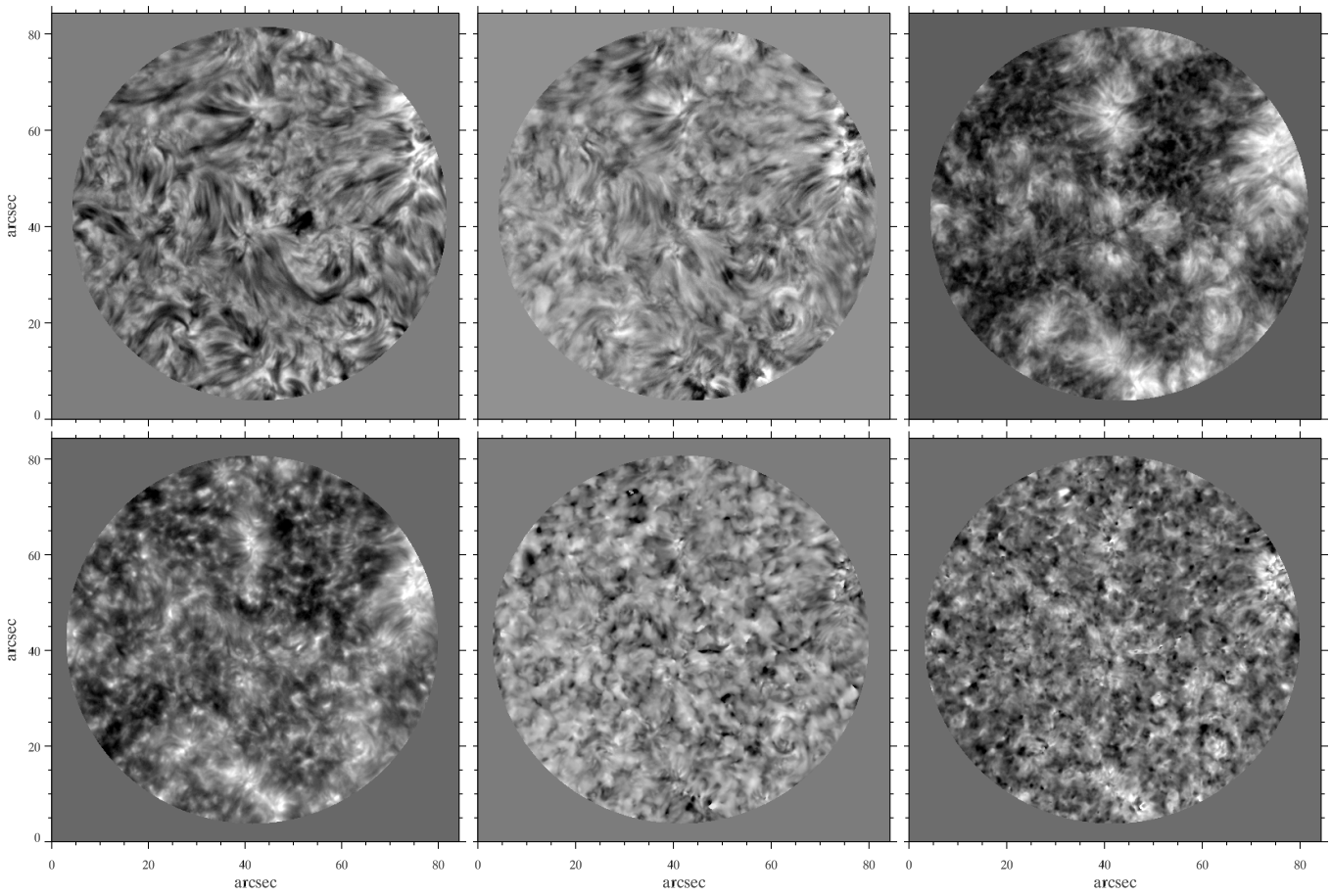

Fig. 3. Image representations of profile measurements at a moment of good seeing (scan No. 11). Solar North is to *the top*, West to *the right*. The greyscale is bytescaled separately for each panel, for the Dopplershifts symmetrically with respect to zero (byte value 127; blueshift black, redshift white). *Upper row*: Hα. *Lower row*: Ca IR. *First column*: minimum intensity per pixel, measured as brightness temperature. *Second column*: Dopplershift of the profile minimum per pixel. *Third column*: core width, measured as in Fig. 2.

coefficient. We show below that the countercorrelation comes from the internetwork shocks.

Much better coherence is shown in the second panel of the second row of Fig. 6 which plots the per-pixel correlation between the two Dopplershift measures. One would not expect such high correlation comparing the center-column images in Fig. 3 since they appear rather dissimilar, but closer inspection shows that indeed the Ca IR Dopplermap has similar fibrils around network as the Hα Dopplermap, although less extended. In the internetwork the former shows many roundish patches that must correlate fairly well with the more fibrilar-shaped Dopplershift features in Hα to produce the good overall correlation in the scatter plot. This correlation may be produced by acoustic shocks seen simultaneously in both lines, or if shocks from below buffet Hα fibrils as suggested by Rutten et al. (2008) or excite local turbulence as suggested by Reardon et al. (2008). The two Dopplermaps so possess larger pixel-by-pixel correlation than cursory inspection suggests, just the opposite of the Hα brightness-Dopplermap comparison.

The remaining two panels in Fig. 3 and the remaining four panels in the lefthand part of Fig. 6 concern the core width measures of the two lines. It is most striking that the Hα width pattern has much larger similarity to the Ca IR minimum intensity than to anything else; this is the key point of this paper. They both show the network as bright patches on a dark background, with longer fibrilar extensions in Hα width than in Ca IR brightness. The internetwork grains stand out more clearly in Ca IR, but there is very good similarity in the underlying internetwork patterns. This large apparent correspondence is confirmed on the pixel-by-pixel level by the second scatter diagram in the bottom row of Fig. 6 which shows both bright-bright and dark-dark correlation with high significance. There is also significant correlation between Ca IR brightness and width and between Hα width and Ca IR width in the first column of Fig. 6. There is no correlation at all between Hα intensity and width, in accordance with the absence of correlation between the two brightness images.

Some peculiar patches appear at times in the Ca IR parameter images. A clear example is given by the feature near (32″, 73″) in Fig. 3, which appears very bright in the minimum-intensity and line-width panels, while being very dark (upflow) with a surprising bright center (downflow) in the Dopplershift map. These features often represent particularly strong internetwork shocks with a strongly asymmetric Ca IR line core profile for which our simple measurements are inadequate. However, such occurrences are rare (much less than one percent), and do not affect the statistical correlations in Fig. 6.

Figure 4 shows temporal averages over the sequence duration of the same quantities as in Fig. 3. Moments of less good seeing were excluded by setting a quality threshold at the mean rms variation of the Hα profile-minimum intensity images, discarding nearly one-third of the samples, spread fairly evenly

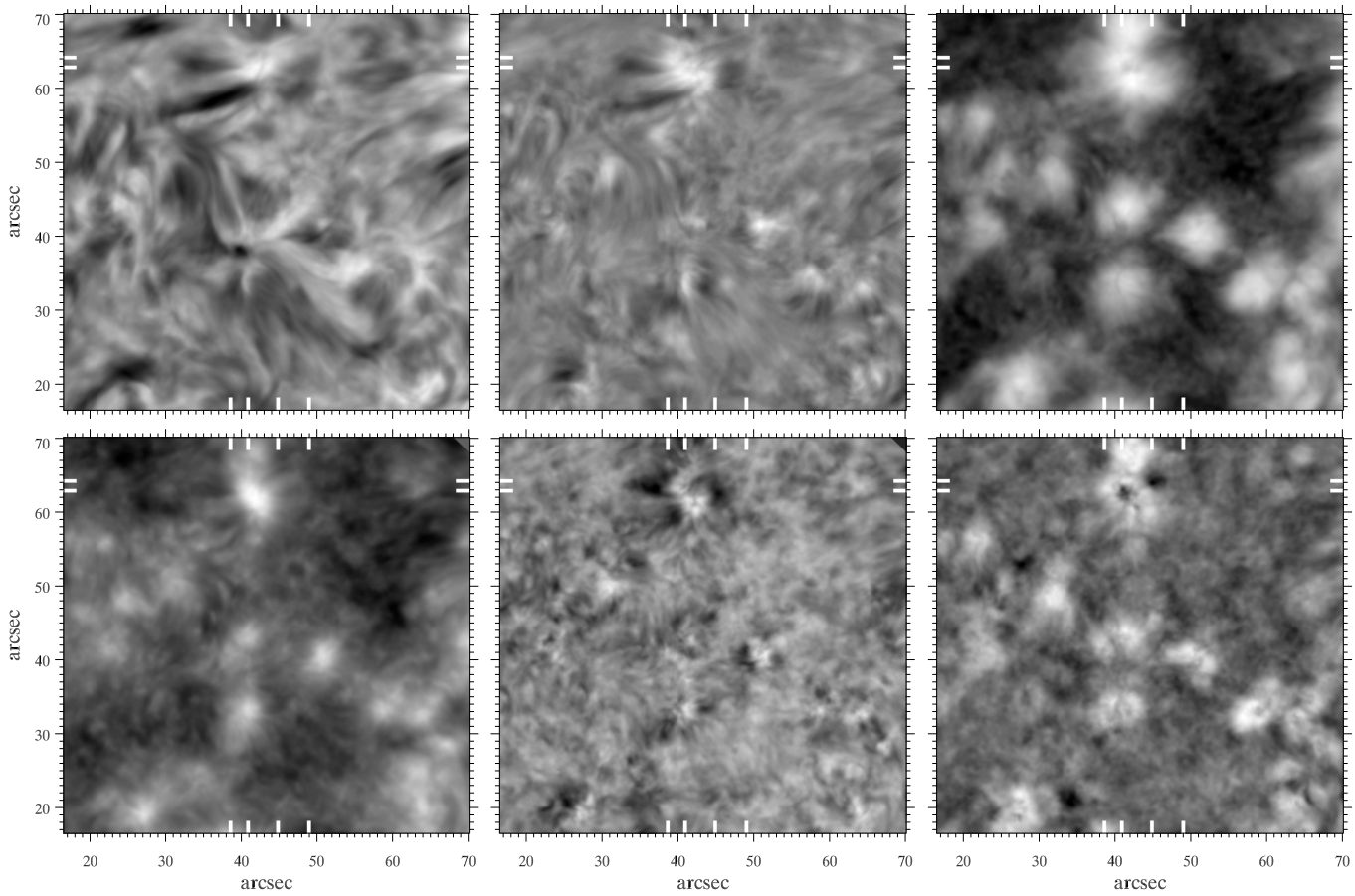

Fig. 4. Temporal averages over the 48-min sequence duration for the central part of the field of view, excluding moments of bad seeing (about one-third of the profile scans). The layout furnishes the same quantities as in Fig. 3. Each panel is bytescaled separately, the Dopplershifts symmetrically with respect to zero. The two markers along the y-axes specify the cut locations used in Fig. 5. They pass through a patch of network area in the center and a weaker field concentration near $x = 63$ arcsec, and through two dark patches of small Ca IR core width in the last panel. The four markers along the x-axes specify pairs of pixels along each cut for which the spectral profile evolution is shown in Fig. 7.

in time. The righthand half of Fig. 6 contains the corresponding pixel-by-pixel scatter plots for the whole IBIS field of view, while only the central part of the field is shown in Fig. 4. This is done to enhance the spatial scale in Fig. 5, which shows the temporal evolution for the pixels along the two fixed-y cuts indicated by the horizontal white markers in Fig. 4. They are selected to pass through the two distinct black patches in the last panel of Fig. 4 and are 1.5 arcsec apart. We describe these figures together.

Figure 5 shows that periodic phenomena abound. All time slices show ubiquitous oscillatory modulation, not only in the internetwork areas but also for the fibrils that jut out from the small area of active network sampled in the middle. The oscillatory signals are most obvious in the Dopplershift patterns (center column) which are remarkably similar for the two lines. They are least clear but still visible in Hα intensity (first panel). They average out when taking a temporal mean, so that the spatial patterns defined by longer-lived structures and motions gain visibility in Fig. 4 in comparison with Fig. 3.

In all measures the internetwork is full of three-minute oscillations with shock signatures, clearest in the Ca IR intensity panels in the form of bright grains (Vecchio et al. 2009). These are comparable to the Ca II H_{2V} and K_{2V} grains reviewed by Rutten & Uitenbroek (1991) and explained by Carlsson & Stein (1997) as steepening and vertically interacting shock waves that travel up until wave conversion occurs at the magnetic canopy (Bogdan et al. 2003). The Hα time slices show that Hα partakes in this three-minute modulation, even in its intensity although that has no resemblance nor correlation to Ca IR in the instantaneous images and scatter diagrams. Further study of this modulation calls for Fourier analysis including phase-difference evaluation with network/internetwork separation following Krijger et al. (2001), which we postpone to a future paper.

The network patch at the center of the time slices shows oscillatory behavior of its own, most clearly in the Dopplershift panels. Some fibrils that jut out from it, especially towards the left in Hα, have alternating flows and may represent dynamic fibrils as described by Hansteen et al. (2006) and De Pontieu et al. (2007a). The central part displays slower undulations as described by Lites et al. (1993). The fibril-dominated regions surrounding the network show a distinctly different behavior than either the nework or internetwork regions, as described by Vecchio et al. (2009).

The temporal averaging in Fig. 4 and the righthand part of Fig. 6 reduces the spread due to these oscillations and other short-lived phenomena, and so serves to enhance longer-term structuring and relationships (note also the reduced ranges of the axes in the right-hand side of Fig. 6). The averaging over the oscillatory components indeed reduces the blue-bright correlation between Ca IR brightness and Dopplershift in the first panel of

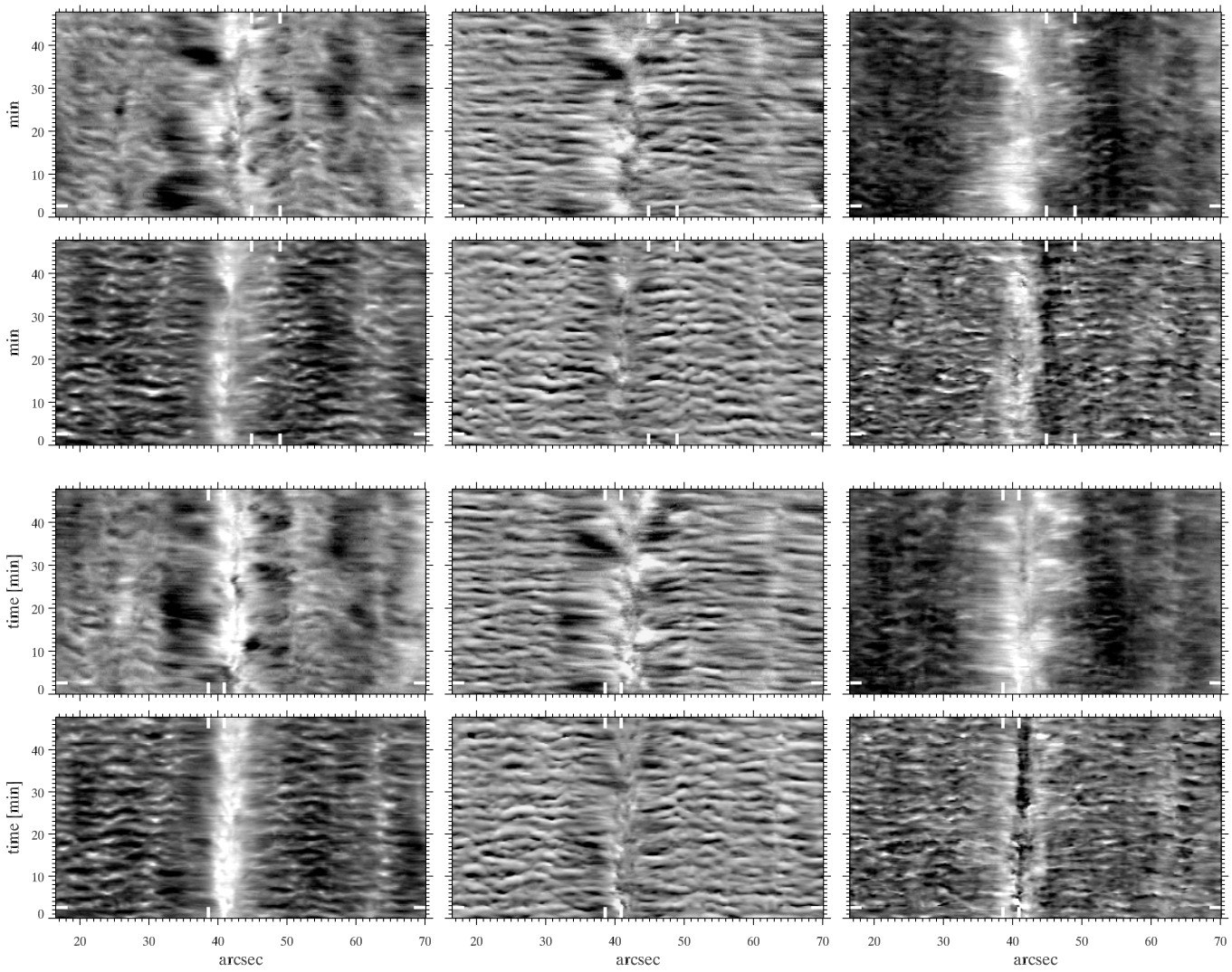

Fig. 5. Space-time slices showing temporal behavior along the two cuts in the x-direction that are defined in Fig. 4 by white horizontal markers along the y-axes. The upper half of this figure corresponds to the higher cut. The six panels per cut show the same quantities as in Figs. 3 and 4. Each panel is bytescaled separately, the Dopplershifts symmetrically with respect to zero. The white markers along the spatial axes specify four pixels, two per slice, for which the spectral profile evolution is shown in Fig. 7. The white markers near the bottom of the time axes specify the moment of observation of the profiles in Fig. 2 and the parameter displays in Fig. 3.

Fig. 6, introduced by internetwork acoustic shocks. In the temporal averaging of the Hα data, the fibril contribution gains dominance and improves the correlation with intensity, corresponding to larger resemblance between the first two Hα panels in Fig. 4 than in Fig. 3.

The scatter plots in the second and third rows of Fig. 6 do not change much in the temporal averaging. The Dopplershifts comparison in the second row looses the internetwork oscillations but maintains fairly good correlation, indicating a correspondence in the fibril flows also seen in the center panels of Fig. 4. In the third row there is slight improvement in the high-high correlation between Ca IR brightness and width.

The most striking change that the temporal averaging brings is increased similarity between the panels relative to the Hα width, Ca IR profile-minimum intensity and Ca IR width of Fig. 4 in comparison with Fig. 3. In particular, the time-averaged Hα width (third panel in upper row) shows a pattern of smooth, bright network aureoles on a dark internetwork background that appears very similar to the Ca IR intensity (first panel in lower row). The bright network patches seem smaller in the latter, but this results from the non-linearity displayed in the last panel of Fig. 6, which quantifies this comparison. It shows high correlation along the whole scatter-sample mountain, but the turnover of the upward tail implies that the brightest network patches appear larger in Hα width. The whole mountain ridge is appreciably narrower in the time-averaged correlation (last panel) than in the instantaneous one (bottom second column). Thus, both network (contributing the upper part) and internetwork (lower part) gain pattern similarity from temporal averaging in this comparison. This tight relationship suggests a common physical origin, which we identify as temperature below. The width-width correlation (bottom panel of the third column in Fig. 6) is just as good as the Hα-width vs. CaII intensity correlation for large core widths but it vanishes for small core widths, indicating that temperature dominates the Ca IR width only when high and that temporal averaging over the internetwork shocks weakens their temperature signature, perhaps through their short duration with respect to their periodicity.

Note that the Ca IR width image in Fig. 4 shows dark centers in some of the bright network patches. The yet brighter network

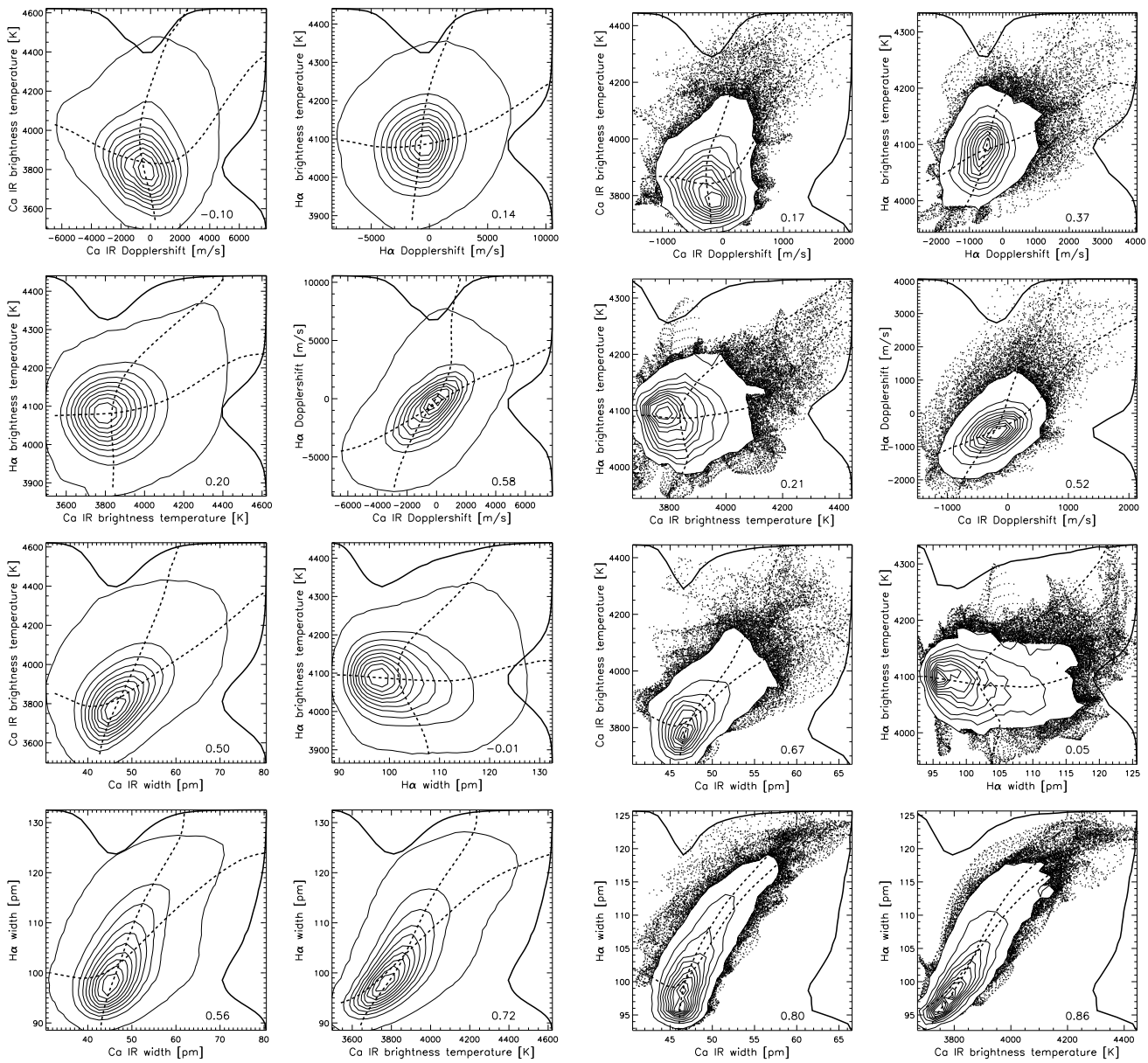

Fig. 6. Scatter-plots between measured quantities for all pixels in the full field of view. The first two columns are instantaneous pixel-by-pixel comparisons between the quantities specified along the axes, for the 66 profile scans with the best seeing (10^7 samples). The third and fourth columns are similar comparisons for the same quantities but temporally averaged over the whole sequence, excluding the third of the scans with the worst seeing (1.6×10^5 samples). The first two columns correspond to Fig. 3, the other two to Fig. 4 but sampling the full field. *Plot format*: to avoid plot saturation, single pixel-by-pixel sample plotting is replaced by plotting sample density contours, except that the extreme individual pixel-by-pixel comparisons beyond the outer contour are shown in Cols. 3 and 4. Extended arcs in these outer scatter clouds come from isolated, non-characteristic features. The solid curves along the top and right sides show the occurrence distribution per quantity. The dashed curves specify the first moments along cuts in each axis direction. They align at perfect correlation (tilt to the upper right) or anticorrelation (tilt to the upper left) and they are perpendicular along the axis directions in the absence of any correlation. The numbers near the lower-right corners specify the overall Pearson correlation coefficient. The intensities of the profile minima are quantified as brightness temperatures. Positive Dopplershift implies downdraft. The scales differ between the instantaneous and sequence-averaged comparisons, especially for Dopplershift. The contours in the latter are noisier due to the smaller statistics. *Top row*: the intensity of the profile minimum against its Dopplershift for Ca IR and Hα. *Second row*: intensity-intensity and Dopplershift-Dopplershift comparisons. *Third row*: minimum intensity against core width for Ca IR and Hα. *Bottom row*: Hα core width against Ca IR core width and against Ca IR minimum intensity.

patches near 2 o'clock and 6 o'clock at the edge of the IBIS field of view, not included in Fig. 4, have similar dark cores. The lower slice in Fig. 5 samples the darkest network core in Fig. 4. The upper slice cuts through a comparably dark feature in Ca IR width that lies adjacent to the network patch. However, comparison of the two dark Ca IR width patches in the time slices in Fig. 5 (the two last panels of each half) suggests that they have intrinsically different nature. The network core patch in the lower panel lies at the center of the fibril rosette and is partially visible also in Hα width. The dark patch adjacent to the network in the upper panel instead seems to be regularly oscillating internetwork, only darker overall.

Figure 7 adds further information on these features by comparing the spectral behavior of the two lines with time,

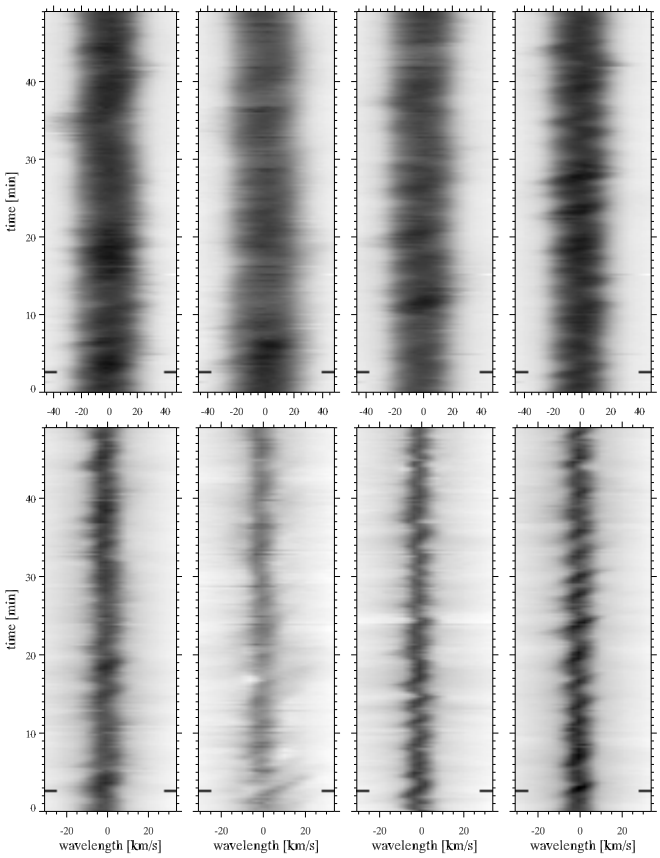

Fig. 7. Spectrum-versus-time plots showing the spectral behavior of Hα (upper row) and Ca IR (lower row) for the four selected pixels specified by markers in Figs. 4 and 5. The wavelengths along the abscissae are expressed as Dopplershift from the nominal line center. The logarithm of the spectral brightness is shown with the same greyscale for all panels along each row; it is logarithmic in order to detail line-core variations, especially for Hα which is too uniformly dark otherwise. The first and second columns are for pixels along the lower cut in Figs. 4 and 5. The first pixel samples normal network, the second the network feature with low Ca IR core width. The third and fourth columns are for pixels along the upper cut and sample the near-network feature with low Ca IR core width and internetwork further away. The black markers near the bottom of each panel specify the time of observation selected in Figs. 2 and 3. The second pixel happened to lie in a dynamic fibril at that moment, causing large Ca IR redshift and blue-wing brightening also seen in Fig. 2.

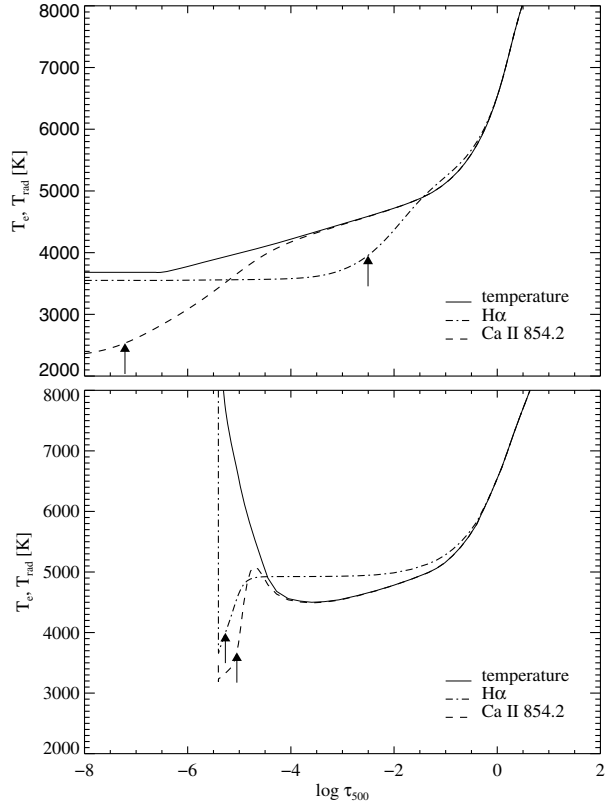

Fig. 8. Demonstration of difference in temperature sensitivity between Ca IR and Hα. Each panel shows the temperature stratification of a standard solar model atmosphere and the resulting total source functions S_λ at the nominal line-center wavelengths for Ca IR and Hα, as function of the continuum optical depth at $\lambda = 500$ nm and with the source functions expressed as formal temperatures through Planck function inversion. The arrows mark $\tau = 1$ locations. *Upper panel*: radiative-equilibrium model KURUCZ from Kurucz (1979, 1992a,b). It was extended outward assuming constant temperature in order to reach the optically thin regime in Ca IR. *Lower panel*: empirical continuum-fitting model FALC of Fontenla et al. (1993). Its very steep transition region lies beyond *the top of the panel* but causes the near-vertical source function increases at *left*.

respectively for pixels within these two dark patches (center columns) and for comparable pixels elsewhere. The two left-most columns sample network pixels, the two right-most ones sample internetwork. The first thing to note about the Hα line core is its much larger width with respect to Ca IR, and its ubiquitous presence (note also that the spectral scale of Fig. 7 differs for the two lines). This basal core width is widest in the first panel, while the superimposed Doppler excursions become a major component only in the internetwork (rightmost columns). The Ca IR core shows these Doppler excursions as well, but more visibly due to its reduced width. Regular shock trains occur most clearly in the internetwork panels for the Ca IR line and are also recognizable in the corresponding Hα panels. In both dark Ca IR-width patches (second and third columns) the Ca IR core indeed appears generally narrower, but also less dark than for the comparison pixels in the first and last columns. Profile inspection along the second column shows that in these pixels Ca IR often has a very shallow chromospheric core for which our width algorithm produces small values.

Finally, we note that the time of observation selected for Fig. 2 happened to sample a feature indicative of dynamic fibrils in the second Ca IR panel of Fig. 7, i.e., displaying large blue-to-red successive shifting in Ca IR. It has correspondingly large redshift and blue-wing brightening in Fig. 2. There is no clear signature of this feature in Hα.

4. Discussion

4.1. Temperature sensitivity

The Ca IR and Hα lines differ in two significant ways in their temperature sensitivity. First, Ca IR is much closer to LTE both with regards to opacity and to source function behavior. The latter difference is demonstrated in Fig. 8 which represents a didactic step beyond the LTE comparison in Fig. 6 of Leenaarts et al. (2006), by comparing standard NLTE formation for the two lines. It shows dramatic difference between the two lines in their sensitivity to the temperature in the outer atmosphere. In each case the lines are computed in NLTE with the RH code

of Uitenbroek (2001), using a sufficiently complete model atom and accounting for coherent scattering in Ly α, Ly β and H & K while assuming complete redistribution for all other lines. In the upper panel, for the KURUCZ radiative-equilibrium model Hα is a deep-photosphere line of which the source function decouples from the Planck function as deep as $\log \tau_{500} \approx 0$, together with the Balmer continuum. The latter, Hα, and Lyα combine together in setting the pertinent hydrogen populations through intricate interactions involving Balmer continuum pumping, Hα photon losses, Rydberg ladder flow, and detailed balancing in Lyα (see Rutten & Carlsson 1994). The Hα source function S_λ closely follows the mean intensity J_λ (not shown) as if it were an ordinary two-level scattering line. Hence, its temperature sensitivity responds mostly to deep-photosphere perturbations. In contrast, the Ca IR line has much larger opacity, so that its source function follows the temperature out to $\log \tau_{500} \approx -4$ before the onset of its scattering drop with $S_\lambda \approx J_\lambda$ which makes the line very dark.

In the lower panel the photospheric part of the FALC temperature stratification is closely the same as the KURUCZ one and so the formation of the lines there remains similar, with thermalization out to $\log \tau_{500} \approx 0$ for Hα and $\log \tau_{500} \approx -4$ for Ca IR. The addition of the FALC chromosphere results in a source function bulge for Ca IR that is familiar from the older explanations of Ca II H & K reversals before partial redistribution and shock dynamics were included (e.g., Fig. 13 of Linsky & Avrett 1970). For Hα, the chromosphere plus transition region act as the addition of a barely opaque, hot, radially inhomogeneous slab well above the photosphere. It raises the scattering source function across the upper photosphere but without giving it sensitivity to the local temperature since there is virtually no local Hα opacity there.

The $\tau = 1$ arrows in Fig. 8 indicate that the predicted line-center brightness temperatures $T_b \approx T_{rad}(\tau_\lambda = 1)$ happen to be nearly equal for Hα at $T_b \approx 3900$ K for both models, but in very different manner. The photosphere-only prediction for Ca IR line-center brightness ($T_b \approx 2500$ K) is instead much lower than with a chromosphere ($T_b \approx 3600$ K). The observed mean values from Fig. 6 are $T_b \approx 4100$ K for Hα and $T_b \approx 3800$ K for Ca IR. Given the very different structure of the source function of the two lines, the closeness of their two brightness temperatures in the model with a chromosphere is more likely a coincidence imposed by the atmospheric model than proof that the lines supply temperature information from the same height in the atmosphere. The Hα line-minimum intensity is much more sensitive to deep-photosphere temperature perturbations, whereas the Ca IR line minimum has more sensitivity to chromospheric temperature perturbations. The first columns of Figs. 3 and 4 confirm this difference dramatically by displaying very dissimilar chromospheric intensity scenes, not only in the instantaneous comparison (Fig. 3) but also in the time-averaged one (Fig. 4). In contrast, the closeness of the formation heights in the chromospheric model suggests that the Dopplershifts and Doppler broadening, which are encoded locally at the last photon scattering independent of the source function nature, should be much more similar. This may explain the larger similarity between the two lines in the corresponding panels of Figs. 3–6. However, the large difference in Hα formation height between the KURUCZ and FALC models on the one hand and the larger apparent extent of fibrils in Hα than in Ca IR in Figs. 3 and 4 on the other hand imply that there is no guarantee of Doppler-encoding similarity between the two lines.

The second major difference between the two lines is that they differ by a factor of 40 in atomic mass. This affects the thermal Doppler broadening and therefore the balance between thermal and nonthermal Doppler broadening of the line profile. The latter was traditionally described by the ad-hoc fudge parameters microturbulence and macroturbulence, with the former entering the Dopplerwidth and the latter applied as Gaussian smearing of the computed emergent line profile. In recent times the usage of these parameters has been replaced by structure-resolving line synthesis from numerical simulations, but so far only for granular convection and magnetoconvection in the low photosphere. Given the low atomic mass, Hα is likely to have thermal broadening dominate over systematic motions, whereas the reverse holds for Ca IR. The spectrum-versus-time displays in Fig. 7 confirm this difference qualitatively. Hence, we attribute the large, generally-present core width of Hα to thermal broadening, and therefore the bright patches in the third panel of Fig. 4 to high temperatures which set the core width locally, at the last scattering. The good correspondence of the Hα line width with the patches of high Ca IR profile-minimum intensity in the fourth panel then results from the appreciable Ca IR source function sensitivity to temperature.

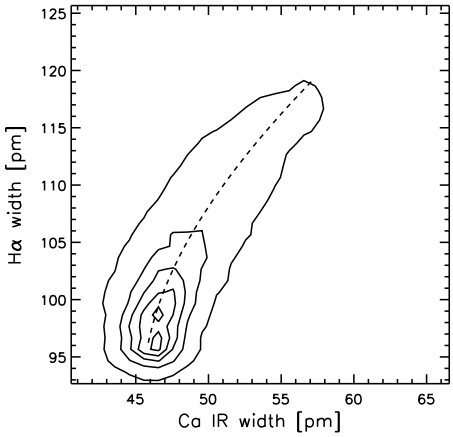

Fig. 9. Width-width correlation between Hα and Ca IR. The contours reproduce every second one in the next-to-last panel of Fig. 6. The dashed curve represents Eq. (1) with best-fit parameters.

Figure 9 quantifies this conclusion in the form of a simple model which reproduces the observed correlation in the next-to-last panel of Fig. 6. The dotted line in figure plots the widths of the two lines against each other that were computed from

$$\Delta\lambda_W \equiv (\lambda/c)\sqrt{v_{therm}^2 + v_{micro}^2 + v_{intrins}^2} \quad (1)$$

for temperature T increasing from $T_{min} = 5000$ K to $T_{max} = 60\,000$ K, a thermal contribution $v_{therm} = \sqrt{2kT/m}$ where k is the Boltzmann constant and m the atomic mass, a microturbulent contribution $v_{micro} = 1 + 10\,(T - T_{min})/(T_{max} - T_{min})$ km s^{-1}, and an intrinsic contribution $v_{intrins}$ set to 43 km s^{-1} for Hα and 16 km s^{-1} for Ca IR. The latter two contributions were adapted to fit the observed correlation. The temperature-dependent microturbulence increases from 1 km s^{-1} to 11 km s^{-1}, in rough agreement with older estimations from ultraviolet line broadening (Canfield & Beckers 1976; Tripp et al. 1978; cf. Fig. 11 of Vernazza et al. 1981). The intrinsic widths represent base contributions making up for the neglect of radiative transfer. Equation (1) may be seen as describing line broadening in a Schuster-Schwarzschild slab or cloud with the irradiative profile and internal line transfer mimicked by these intrinsic widths. It is only a simple ad-hoc fit, but it demonstrates that the observed mean width-width correlation in Fig. 6 may be attributable to temperature. The value $T_{max} = 60\,000$ K seems

very high in comparison with standard one-dimensional models in which both hydrogen and once-ionized calcium are fully ionized at such temperatures, but observations as in Fig. 13 of Rutten (2007) suggest the presence of Hα even at very high temperature.

Note that such core width behavior cannot be reproduced by specification of a deeper temperature rise as done by Fontenla et al. (1993). Their A, C, ..., F and P models were designed to represent progressively hotter chromospheres in quiet cell interior, average quiet sun, network, and plage by placing the chromospheric temperature rise at increasingly larger column mass. However, when measuring with our method the line widths from profiles synthesized in NLTE (as in Fig. 8), this sequence produces smaller core width with increasing activity instead of the actual core-width increase we observe.

4.2. Chromospheric heating

The demonstrations above make us conclude that the high correlation between time-averaged Hα core width and Ca IR line-minimum intensity represents common sensitivity to temperature. Hence, the network patches display excess heat. The general, basal presence of a wide Hα core in the first columns of Fig. 7, as well as the large Hα widths ubiquitously present in the network in Fig. 5 indicate that this heating is rather constant in time in the magnetic concentrations. Temporal averaging over episodes of strong heating occurring at the base of the fibrils jutting out from the network (cf. the rightmost panels of Fig. 5) produces the smooth bright network aureoles in the third panel of Fig. 4. The dark network patch of small Ca IR width sampled in Figs. 5 and 7 indicate reduce core-widths related to a significant weakening of the line core, likely marking maximum heating at the center of the network patch.

The calculated fit to the width-width correlation in Fig. 9 includes a sizable microturbulence component which scales with temperature. Its necessity suggests the action of unresolved waves. Perhaps these are the ones affecting or producing the "straws" or "spicules-II" observed in Ca II H, respectively near the limb by Rutten (2006) and across the limb by De Pontieu et al. (2007b), that were interpreted as Alfvén waves by De Pontieu et al. (2007c). They may also explain unresolved ultraviolet line broadening (McIntosh et al. 2008) and the "rapid blueshift events" at the edge of network concentrations reported by Langangen et al. (2008). It is also interesting to note that the higher-temperature regions (i.e. network and fibrils) display a stronger turbulence spectrum of the Ca IR velocity than the internetwork (Reardon et al. 2008).

The similarity between Hα width and Ca IR intensity extends to the oscillation sequences in the internetwork areas in Fig. 5. The Hα width shows internetwork grains less markedly than Ca IR intensity, but it follows the same modulation. The bright phases may therefore be interpreted as localized temperature increases, but the overall darkness of the internetwork in Fig. 4 implies less total heating than in the network. The dark, near-network patch in Ca IR width sampled in Figs. 5 and 7 also seems to have smaller Ca IR width from being brighter than the comparison internetwork pixel, perhaps from more sub-canopy heating so close to network.

4.3. Future interpretation

The next step in profile interpretation is to distill more intrinsic line formation parameters. Traditionally, chromospheric fine structure is described through cloud modeling (see review by Tziotziou 2007). In its most basic form it delivers the four parameters: optical thickness, source function (sometimes parabolic), Dopplershift, and Dopplerwidth for a homogeneous cloud irradiated from below. Our finding that in particular Hα profile-minimum intensity has no correlation with the actual temperature (as sampled by Hα width) nor with the instantaneous Hα Dopplershift implies that the rich fibrilar structure displayed by this line in narrow-band filtergrams is indeed a complex mixture of all four parameters. A complication adding uncertainty is the required specification of the Hα profile in the cloud irradiation from below and aside. Figure 8 suggests that combination of radiative-equilibrium modeling with back-radiation from the cloud may serve as first approximation.

Granted cloud-model determinations of these four parameters, the next issue is how to interpret the cloud source function. Already in his original formulation for off-limb spicules, Beckers (e.g., Beckers 1964, 1968, 1972) converted the basic empirical cloud parameters into density and temperature through the tables of Giovanelli (1967) for NLTE hydrogen ionization. More recent reformulations of this approach (e.g., Alissandrakis et al. 1990; Tsiropoula & Schmieder 1997) have generally been replaced by large-volume NLTE line profile computation followed by data "inversion" through best-fit parameter adaptation (see Tziotziou 2007, for references). However, Leenaarts et al. (2007) have undermined this technique by finding that in chromospheric structures which suffer repetitive episodic heating, the actual populations of the atomic levels governing Hα can be very far from time-independent statistical equilibrium. Since shocks seem ubiquitously present in the chromosphere (center column of Fig. 5), Hα cloud-model interpretation needs to be reformulated including time-dependent hydrogen balancing. A first approximation may be to maintain the high degree of ionization and the corresponding large Hα population fractions reached at moments of high temperature.

Obviously, it will be even better to compare data as ours directly to numerical spectral line synthesis employing ab-initio MHD simulations of time-dependent chromospheric fine structure, such the recent one including Ca IR formation by Leenaarts et al. (2009) but yet lacking chromospheric fibrils comparable to the observed ones. When realistic fibrils arise and are combined with proper Ca IR and Hα synthesis, reproducing the scatter diagrams in Fig. 6 will provide an excellent proving ground.

5. Conclusion

Imaging spectroscopy with IBIS provides diagnostics well beyond slit-limited spectroscopy or bandpass-limited filter imaging. The long-duration simultaneous Ca IR and Hα profile-resolved IBIS sequences presented here give direct evidence of chromospheric heating in network. The clincher measurement is the Hα core width.

The network heating appears to occur fairly continuously and to affect also the nearby base of fibrilar features jutting out from it, but it does not extend as far as, nor shows the fibrilar fine structure of, the petals of classical rosettes in Hα filtergrams. Their visibility arises from complex combinations of Doppler width, Dopplershift, optical thickness, and source function variations, without direct coupling to fibril temperature. In contrast, the striking correspondence between Hα core width and Ca IR line-minimum brightness (Figs. 4 and 6) proves that the latter is a better temperature proxy. The best, however, is the Hα core width.

Acknowledgements. We are much indebted to DST observers Mike Bradford, Joe Elrod and Doug Gilliam. IBIS was constructed by INAF/OAA with contributions from the University of Florence, the University of Rome, MIUR, and MAE, and is operated with support of the National Solar Observatory. The NSO is operated by the Association of Universities for Research in Astronomy, Inc., under cooperative agreement with the National Science Foundation. R. J. Rutten, G. Cauzzi, and K. P. Reardon thank the National Solar Observatory/Sacramento Peak for their ever-present hospitality, and the Leids Kerkhoven-Bosscha Fonds for travel support. This research made much use of NASA's Astrophysics Data System.

References

Alissandrakis, C. E., Tsiropoula, G., & Mein, P. 1990, A&A, 230, 200
Beckers, J. M. 1964, A Study of the Fine Structures in the Solar Chromosphere, AFCRL Environmental Research Paper No. 49, Ph.D. Thesis Utrecht University
Beckers, J. M. 1968, Sol. Phys., 3, 367
Beckers, J. M. 1972, ARA&A, 10, 73
Bello González, N., & Kneer, F. 2008, A&A, 480, 265
Bogdan, T. J., Carlsson, M., Hansteen, V. H., et al. 2003, ApJ, 599, 626
Canfield, R. C., & Beckers, J. M. 1976, in Physique des Mouvements dans les Atmospheres, ed. R. Cayrel, & M. Steinberg, 291
Carlsson, M. 2007, in The Physics of Chromospheric Plasmas, ed. P. Heinzel, I. Dorotovič, & R. J. Rutten, ASP Conf. Ser., 368, 49
Carlsson, M., & Stein, R. F. 1997, ApJ, 481, 500
Cauzzi, G., Reardon, K. P., Uitenbroek, H., et al. 2008, A&A, 480, 515
Cavallini, F. 2006, Sol. Phys., 236, 415
De Pontieu, B., Hansteen, V. H., Rouppe van der Voort, L., van Noort, M., & Carlsson, M. 2007a, ApJ, 655, 624
De Pontieu, B., McIntosh, S., Hansteen, V. H., et al. 2007b, PASJ, 59, 655
De Pontieu, B., McIntosh, S. W., Carlsson, M., et al. 2007c, Science, 318, 1574
Fontenla, J. M., Avrett, E. H., & Loeser, R. 1993, ApJ, 406, 319
Giovanelli, R. G. 1967, Aust. J. Phys., 20, 81
Hansteen, V. H., De Pontieu, B., Rouppe van der Voort, L., van Noort, M., & Carlsson, M. 2006, ApJ, 647, L73
Hasan, S. S., & van Ballegooijen, A. A. 2008, ApJ, 680, 1542
Judge, P. 2006, in Solar MHD Theory and Observations: a High Spatial Resolution Perspective, ed. J. Leibacher, R. F. Stein, & H. Uitenbroek, ASP Conf. Ser., 354, 259
Judge, P. G., & Peter, H. 1998, Space Sci. Rev., 85, 187
Krijger, J. M., Rutten, R. J., Lites, B. W., et al. 2001, A&A, 379, 1052
Kurucz, R. L. 1979, ApJS, 40, 1
Kurucz, R. L. 1992a, Rev. Mex. Astron. Astrofis., 23, 181
Kurucz, R. L. 1992b, Rev. Mex. Astron. Astrofis., 23, 187
Langangen, Ø., De Pontieu, B., Carlsson, M., et al. 2008, ApJ, 679, L167
Leenaarts, J., Rutten, R. J., Sütterlin, P., Carlsson, M., & Uitenbroek, H. 2006, A&A, 449, 1209
Leenaarts, J., Carlsson, M., Hansteen, V., & Rutten, R. J. 2007, A&A, 473, 625
Leenaarts, J., Carlsson, M., Hansteen, V., & Rouppe van der Voort, L. 2009, ApJ, 694, L128
Linsky, J. L., & Avrett, E. H. 1970, PASP, 82, 169
Lites, B. W., Rutten, R. J., & Kalkofen, W. 1993, ApJ, 414, 345
McIntosh, S. W., De Pontieu, B., & Tarbell, T. D. 2008, ApJ, 673, L219
Neckel, H. 1999, Sol. Phys., 184, 421
Reardon, K. P., & Cavallini, F. 2008, A&A, 481, 897
Reardon, K. P., Lepreti, F., Carbone, V., & Vecchio, A. 2008, ApJ, 683, L207
Reardon, K. P., Uitenbroek, H., & Cauzzi, G. 2009, A&A, 500, 1239
Rimmele, T. R. 2004, SPIE, 5490, 34
Rouppe van der Voort, L. H. M., De Pontieu, B., Hansteen, V. H., Carlsson, M., & van Noort, M. 2007, ApJ, 660, L169
Rutten, R. J. 2006, in Solar MHD Theory and Observations: a High Spatial Resolution Perspective, ed. J. Leibacher, R. F. Stein, & H. Uitenbroek, ASP Conf. Ser., 354, 276
Rutten, R. J. 2007, in The Physics of Chromospheric Plasmas, ed. P. Heinzel, I. Dorotovič, & R. J. Rutten, ASP Conf. Ser., 368, 27
Rutten, R. J., & Carlsson, M. 1994, in Infrared Solar Physics, ed. D. M. Rabin, J. T. Jefferies, & C. Lindsey, IAU Symp., 154, 309
Rutten, R. J., & Uitenbroek, H. 1991, Sol. Phys., 134, 15
Rutten, R. J., van Veelen, B., & Sütterlin, P. 2008, Sol. Phys., 251, 533
Scharmer, G. B. 2006, A&A, 447, 1111
Tripp, D. A., Athay, R. G., & Peterson, V. L. 1978, ApJ, 220, 314
Tsiropoula, G., & Schmieder, B. 1997, A&A, 324, 1183
Tziotziou, K. 2007, in The Physics of Chromospheric Plasmas, ed. P. Heinzel, I. Dorotovič, & R. J. Rutten, ASP Conf. Ser., 368, 217
Uitenbroek, H. 2001, ApJ, 557, 389
van Noort, M. J., & Rouppe van der Voort, L. H. M. 2006, ApJ, 648, L67
Vecchio, A., Cauzzi, G., Reardon, K. P., Janssen, K., & Rimmele, T. 2007, A&A, 461, L1
Vecchio, A., Cauzzi, G., & Reardon, K. P. 2009, A&A, 494, 269
Vernazza, J. E., Avrett, E. H., & Loeser, R. 1981, ApJS, 45, 635
Wallace, L., Hinkle, K., & Livingston, W. 1998, an Atlas of the Spectrum of the Solar Photosphere from 13 500 to 28 000 cm^{-1} (3570 to 7405 Å) Technical Report 98-001, National Solar Observatory, Tucson